





11 **Abstract**

12 To facilitate the future inclusion of aerosol-radiation interactions in the regional  
13 operational Numerical Weather Prediction (NWP) system – RMAPS-ST (adapted  
14 from Weather Research and Forecasting, WRF) at the Institute of Urban  
15 Meteorology (IUM), China Meteorological Administration (CMA), the impacts of  
16 aerosol-radiation interactions on the forecast of surface radiation and meteorological  
17 parameters during a heavy pollution event (December 6<sup>th</sup> -10<sup>th</sup>, 2015) over northern  
18 China were investigated. The aerosol information was simulated by RMAPS-Chem  
19 (adapted from WRF model coupled with Chemistry, WRF-Chem) and then  
20 offline-coupled into Rapid Radiative Transfer Model for General Circulation Models  
21 (RRTMG) radiation scheme of WRF to enable the aerosol-radiation feedback in the  
22 forecast. To ensure the accuracy of high-frequency (hourly) updated aerosol optical  
23 depth (AOD) field, the temporal variations of simulated AOD at 550nm were  
24 evaluated against satellite and in-situ observations, which showed great consistency.  
25 Further comparison of PM<sub>2.5</sub> with in-situ observation showed WRF-Chem  
26 reasonably captured the PM<sub>2.5</sub> field in terms of spatial distribution and magnitude,  
27 with the correlation coefficients of 0.85, 0.89 and 0.76 at Beijing, Shijiazhuang and  
28 Tianjin, respectively. Forecasts with/without the hourly aerosol information were  
29 conducted further, and the differences of surface radiation, energy budget, and  
30 meteorological parameters were evaluated against surface and sounding  
31 observations. The offline-coupling simulation (with aerosol-radiation interaction



32 active) showed a remarkable decrease of downward shortwave (SW) radiation  
33 reaching surface, thus helping to reduce the overestimated SW radiation during  
34 daytime. The simulated surface radiation budget was also improved, with the biases  
35 of net surface radiation decreased by 85.3%, 50.0%, 35.4%, and 44.1% during  
36 daytime at Beijing, Tianjin, Taiyuan and Jinan respectively, accompanied by the  
37 reduction of sensible ( $16.1 \text{ W m}^{-2}$ , 18.5%) and latent ( $6.8 \text{ W m}^{-2}$ , 13.4%) heat fluxes  
38 emitted by the surface at noon-time. In addition, the cooling of 2-m temperature  
39 ( $\sim 0.40 \text{ }^\circ\text{C}$ ) and the decrease of horizontal wind speed near surface ( $\sim 0.08 \text{ m s}^{-1}$ )  
40 caused by the aerosol-radiation interaction over northern China helped to reduce the  
41 bias by  $\sim 73.9\%$  and  $\sim 7.8\%$  respectively, particularly during daytime. Further  
42 comparisons indicated that the simulation implemented AOD could better capture  
43 the vertical structure of atmospheric wind. Accompanied with the lower planetary  
44 boundary layer and the increased atmospheric stability, both U and V wind at  
45 850hPa showed the convergence which were unfavorable for pollutants dispersion.  
46 Since RMPAS-ST provides meteorological initial condition for RMPS-Chem, the  
47 changes of meteorology introduced by aerosol-radiation interaction would routinely  
48 impact the simulations of pollutants. These results demonstrated the profound  
49 influence of aerosol-radiation interactions on the improvement of predictive  
50 accuracy and the potential prospects to offline couple near-real-time aerosol  
51 information in regional RMAPS-ST NWP in northern China.

52 **Key words:** Aerosol-radiation interactions, offline-coupling, WRF, northern China,

<https://doi.org/10.5194/acp-2019-1056>  
This is just a preview and not the published preprint.  
© Author(s) 2020. CC-BY 4.0 License.



53 pollution



54 **1. Introduction**

55 Aerosol-radiation interactions modify the radiative energy budget of the  
56 earth-atmosphere system through the interaction between aerosols and solar radiation  
57 by scattering and absorbing mechanism as well as the absorption and emitting of  
58 thermal radiation (Ramanathan et al., 2001; Yu et al., 2006). The aerosol-radiation  
59 interaction may cool or heat the earth-atmosphere system, alter surface and  
60 atmospheric radiation and temperature structure on regional and global climate, which  
61 have been widely reported and studied (Hansen et al., 1997; Ramanathan et al., 2001;  
62 Kaufman et al., 2002; Liao et al., 2006; Zhang et al., 2010; Ghan et al., 2012; Yang et  
63 al., 2017a). Considering the lifetime of most aerosol particles and their locally uneven  
64 distribution, as well as their high dependence on emission sources and local  
65 meteorological conditions for dispersion (Rodwell and Jung, 2008; Liu et al., 2012;  
66 Liao et al, 2015), the impacts of aerosol in short durations over regional areas are  
67 worthy of more concerns (Cheng et al., 2017; Zheng et al., 2019).

68 With substantial aerosol loading, aerosol particles have significant influences on  
69 meteorology, and many endeavors by both field experiments and numerical models  
70 have been devoted to study the impacts of aerosol-radiation interaction on  
71 meteorological fields, including surface solar radiation, planetary boundary layer  
72 (PBL), atmospheric heating rate, atmospheric stability (Hansen et al., 1997; Ackerman  
73 et al., 2000; Quan et al., 2014; Yang et al., 2017b; Wang et al., 2018), cloud formation  
74 due to thermodynamic changes, and further the onset or reduction of precipitation



75 systems (Grell et al., 2011; Guo et al., 2016). For instance, in worldwide, the  
76 simulations with Weather Research and Forecasting (WRF) model coupled with  
77 Chemistry (WRF-Chem) showed that by purely taking into account the  
78 aerosol-radiation interactions, aerosols may reduce incoming solar radiation by up to  
79 -9% (-16%) and 2-m temperatures by up to 0.16°C (0.37°C) in January (July) over  
80 the continental U.S. (Zhang et al., 2010), affect meso-scale convection system owing  
81 to thermodynamic changes over Atlantic Ocean during Saharan dust eruption period  
82 (Chen et al., 2017), and lead to the distinct changes in precipitation due to the changes  
83 in temperature profile and stabilities induced by the aerosol-radiation interaction over  
84 Eastern China (Huang et al., 2016).

85 Northern China is experiencing heavy air pollution in past two decades, with  
86 particle matter (PM) being the primary pollutant, particularly during wintertime (Chan  
87 and Yao, 2008; Zhang et al., 2015; Zhao et al., 2019) due to the combination of high  
88 primary and precursor emissions and frequent stable meteorological conditions in this  
89 area (Elser et al., 2016; Zhang et al., 2018). The effects of aerosol-radiation interaction  
90 on meteorology were expected to be much more significant over northern China.  
91 Applying WRF and Community Multi-scale Air Quality Model (CMAQ) system  
92 (WRF-CMAQ), Wang et al. (2014) and Sekiguchi et al. (2018) reported a 53%  
93 reduction in solar radiation reaching surface and ~100m decrease of planetary  
94 boundary layer height (PBLH) in response to the presence of aerosols during a severe  
95 winter haze episode in China. Wang et al. (2015a, b) used the online chemical weather



96 forecasting mode Global/Regional Assimilation and PrEdiction System/ Chinese  
97 Unified Atmospheric Chemistry Environment (GRAPES/CUACE) and illustrated that  
98 the solar radiation at ground decreased by 15% in Beijing–TianJin–Hebei, China, and  
99 its near surroundings, accompanied by the decrease in turbulence diffusion of about  
100 52% and a decrease in PBLH of about 33 % during a haze episode of summertime in  
101 2008.

102 Considering the significant influence of the aerosol-radiation interaction on  
103 meteorological forecasts as illustrated in many studies (Kaufman et al., 2002; Zhang  
104 et al., 2010), several weather forecast centers are conducting research to facilitate  
105 more complex aerosol information inclusion in operational numerical weather  
106 prediction (NWP) models. For example, Rodwell and Jung (2008) showed the local  
107 medium-range forecast skills were improved due to the application of new  
108 climatological aerosol distribution in European Centre for Medium-Range Weather  
109 Forecasts (ECMWF). Recently, a positive impact up to a 48h lead time on the 2m  
110 temperature and forecasts of surface radiative fluxes were reported in ECMWF by  
111 applying the prognostic aerosols compared to the monthly climatological aerosol  
112 (Rémy et al., 2015). Toll et al. (2016) found that the inclusion of aerosol effects in  
113 NWP system was beneficial to the accuracy of simulated radiative fluxes, temperature  
114 and humidity in the lower troposphere over Europe. In addition, it was shown that the  
115 quality of weather forecasts at UK MET office can be further advanced when the  
116 real-time aerosol distribution rather than climatological distribution were included,



117 with the decreased bias of downward SW at surface ( $-2.79 \text{ W m}^{-2}$  vs.  $-5.30 \text{ W m}^{-2}$ )  
118 and the mean sea-level pressure (0.71hPa vs. 0.80hPa) (Mulcahy et al., 2014; Toll et  
119 al., 2015). For these research serving for operational NWP systems, offline approach  
120 (that aerosol information were simulated by separate chemistry system and then  
121 offline coupled to NWP model) were mostly used.

122 In most previous research-targeted modeling studies over northern China, the  
123 aerosol-radiation interaction has been widely accessed in online-coupled  
124 meteorology-chemistry models, which might not be practical for NWP purpose.  
125 Considering aerosol particles differ by morphology, size and chemical composition,  
126 therefore, the numerical treatment of aerosol particles in atmospheric models needs  
127 sophisticated method and considerable simplifications, which may bring in more  
128 assumptions and uncertainties in online coupling (Baklanov et al., 2014). Moreover,  
129 the online simulations require quite high computational costs and could not meet the  
130 requirement of efficiency for operational NWP. Grell and Baklanov (2011) illustrated  
131 that the offline approach could generate to almost identical results compared to online  
132 simulation with the offline-coupling intervals about 0.5-1h. Thus, the  
133 computational-economic offline simulation provides a feasible and computationally  
134 less demanding approach to include the aerosol-radiation interaction in an operational  
135 NWP system. Péré et al. (2011) adopted an offline-coupling between the  
136 chemistry-transport model CHIMERE and WRF to study the radiative forcing of high  
137 load aerosols during the heat wave of summer in 2003 over Western Europe. Wang et



138 al. (2018) offline implemented the daily AOD from Moderate Resolution Imaging  
139 Spectroradiometer (MODIS) to WRF during a heavy winter pollution at Beijing to  
140 study the effect of aerosols on boundary layer. Still, there have been few studies that  
141 adopted offline simulation to investigate the impacts of aerosol-radiation interactions  
142 over northern China on NWP system. At Institute of Urban Meteorology, regional  
143 operational NWP system–RMAPS-ST (adapted from WRF) and regional air quality  
144 model–RMPSA-Chem (adapted from WRF-Chem) were applied operationally. In this  
145 study, we investigate the radiative effects of aerosols and their feedbacks on weather  
146 forecasting over northern China during a polluted event occurred in winter of 2015,  
147 and further potential impacts of changed meteorology to the transport and dissipation  
148 of pollution. The simulations were in the configurations of the two systems, aiming at  
149 presenting the offline-coupling of the high-frequent real-time aerosol distribution  
150 simulated by WRF-Chem and WRF, and evaluating the potential effects of  
151 aerosol-radiation interactions on the forecast skills in the RMAPS-ST system for  
152 future purpose.

153 The remainder of the paper was organized as follows. Section 2 presented the  
154 model configuration and experimental design. In section 3, the model’s capabilities in  
155 capturing and forecasting the pollution episode were validated with observations first,  
156 and impacts of aerosol-radiation interactions on meteorological forecasting over  
157 northern China were analyzed further. The final section provided the concluding  
158 remarks.



## 159 2. Model description and experimental design

160 WRF is a state-of-the-art atmospheric modeling system designed for both  
161 meteorological research and NWP. The WRF version 3.8.1 released in August, 2016  
162 was used in this study for a domain covering the northern China with a horizontal  
163 resolution of 9km ( $222 \times 201$  grid points, Fig. 1a), and for 50 vertical levels. The  
164 lateral boundary conditions (BCs) and initial conditions (ICs) for meteorological  
165 variables are provided by the forecast of ECMWF. The major physical schemes  
166 include the Assymetric Convective Model Version 2 (ACM2) PBL scheme (Pleim,  
167 2007), the Thompson microphysics without aerosol-aware option (Thompson et al.,  
168 2008), the Kain-Fritsch cumulus parameterization (Kain, 2004), and the Natioal  
169 Center for Envirometal Prediction, Oregon State University, Air Force, and  
170 Hydrologic Research Lab's (NOAH) land-surface module (Chen and Dudhia, 2001;  
171 Ek et al., 2003). The landuse data have been reprocessed, which has a higher  
172 accuracy and finer classification for urban areas (Zhang et al., 2013) and the urban  
173 canopy model (UCM) was not actived.

174 The shortwave and longwave radiation scheme is Rapid Radiative Transfer  
175 Model for General Circulation Models (RRTMG) (Iacono et al., 2008). RRTMG  
176 scheme is a new version of RRTM added in Version 3.1, and includes the Monte  
177 Carlo Independent Column Approximation (MCICA) method of random cloud  
178 overlap. A recent intercomparison study showed that RRTMG had relatively smaller  
179 mean errors in solar flux at the surface and the top of the atmosphere (Oreopoulos et



180 al., 2012) and was considered as recommended WRF configuration for air quality  
181 modeling (Rogers et al., 2013). RRTMG scheme is capable to include the  
182 climatological aerosol data with spatial and temporal variations or an external time  
183 varying 3D aerosol input through the option of AER\_OPT (Ruiz-Arias et al., 2014).  
184 In the present study, the real-time hourly aerosol optical depth (AOD) at 550nm  
185 from external files were input into WRF following the second approach. The AOD  
186 at 550nm was calculated as the vertical intergration of extinction coefficients at  
187 550nm from WRF-Chem simulation.

188 WRF-Chem version 3.3.1 was applied in this study, and the horizontal  
189 resolution was 9 km, with 222×201 grid points covering northern China, which were  
190 the same as configurations of WRF mentioned above. WRF-Chem simulates the  
191 formation, transformation and transport processes of both primary and secondary  
192 atmospheric pollutants, including gases and PM species (Zhao et al., 2019). Physical  
193 parameterizations included single-layer Urban Canopy Model, Noah land-surface,  
194 Yonsei University (YSU) PBL, Grell-Devenyi ensemble convection, Thompson  
195 microphysics, and RRTM longwave and Goddard shortwave radiation (Chen and  
196 Dudhia, 2001; Hong et al., 2006; Grell and Dévényi, 2002; Thompson et al., 2008;  
197 Mlawer et al., 1997; Chou and Suarez, 1999). Carbon bond mechanism Z (CBMZ)  
198 including comprehensive reactions and alterable scenarios were used as the  
199 gas-phase mechanism. Model for Simulating Aerosol Interactions and Chemistry  
200 (MOSAIC) are used with four size bins (Zaveri and Peters, 1999). Anthropogenic



201 emission data were from the MEIC (2012) inventory (<http://www.meicmodel.org/>)  
202 with a resolution of  $0.1^{\circ} \times 0.1^{\circ}$ . Meteorological ICs and BCs were obtained from the  
203 Final Analysis data (FNL) with a resolution of  $1.0^{\circ} \times 1.0^{\circ}$  from the National Centers  
204 for Environmental Prediction (NCEP). To generate aerosol fields for study period  
205 (Dec. 2<sup>nd</sup>-11<sup>th</sup>), 9-days WRF-Chem simulations from Dec. 2<sup>nd</sup> were conducted using  
206 prescribed idealized profiles as ICs and BCs for chemical species.

207 To estimate the aerosol radiative forcing and its feedbacks on meteorological  
208 fields, two sets of 24-hour WRF forecasts were conducted at 00UTC from 2<sup>nd</sup>-10<sup>th</sup>  
209 December 2015 with WRF-Chem simulated AOD fields as input fields. The only  
210 difference between the two sets of forecasts is whether the aerosol radiative  
211 feedback is activated (Aero) or not (NoAero), and other schemes remained the same.

212 The sites of observations over simulated domain and northern China plain (NCP,  
213 purple box in Fig. 1a) are shown in Fig. 1. Since the AOD provided by MODIS  
214 instruments on-board NASA polar orbiting satellites Aqua and Terra are both not  
215 available in the region with high pollution, three sites of AErosol Robotic NETwork  
216 (AERONET) are used to validate the simulation (black dots in Fig. 1b), and the  
217 observed AOD obtained from observation at the Institute of Atmospheric Physics  
218 (IAP), Chinese Academy of Sciences ( $39^{\circ}58' 28''$  N,  $116^{\circ}22' 16''$  E) in Beijing  
219 city (blue dot in Fig. 1b) is also included as supplementary. The hourly observed  
220  $PM_{2.5}$  concentrations of total 813/332 monitoring stations over the study  
221 domain/NCP were from the released data by the China National Environmental



222 Monitoring Centre (<http://106.37.208.233:20035/>, colored dots in Fig. 3a). For given  
223 cities (dots in Fig. 1a), hourly  $PM_{2.5}$  concentration was represented by the average of  
224 data from all monitoring sites located in the city. Simulated meteorological variables  
225 including 2-m temperature and wind speed at 10m were evaluated using in-situ  
226 observations from National Meteorological Information Center  
227 (<http://data.cma.cn/data/cdcindex.html>) of China Meteorological Administration  
228 (CMA, dots in Fig. 8a). The radiations were observed at IAP and in-situ stations of  
229 CMA (shown as triangles in Fig. 1a). The vertical observation of atmospheric wind  
230 speed from sounding were also used (circles in Fig. 1a). The variables, sources,  
231 numbers of sites in the domain and NCP and the frequency of chemical and  
232 meteorological observations were also listed in Table 1.

### 233 3. Results

#### 234 3.1 Evaluation of AOD and $PM_{2.5}$ simulated by WRF-Chem

235 Before the offline-coupling of the WRF-Chem simulated hourly AOD to  
236 meteorological model WRF, we first validated the simulated AOD and ensured the  
237 model's capability to reproduce the features of the aerosol field. Figure 2 displayed  
238 the temporal variation of simulated AOD at 550nm (blue solid) at four sites, in  
239 comparison with three AERONET stations (black circles in Figs. 2a-c) and IAP site  
240 (black circles in Fig. 2d) for the period during 3<sup>rd</sup> to 11<sup>th</sup> Dec, 2015 (local time, LT).  
241 As shown in blue solids in Fig. 2a, the simulated AOD increased since 6<sup>th</sup> Dec. and  
242 reached the peak value of 9 on 7<sup>th</sup>, and the high AOD value maintained until 9<sup>th</sup> and



243 reached the second peak. The second peak was also observed from AERONET  
244 though most of them were missing during the pollution event. The temporal  
245 variations of AOD at Beijing-CMA and IAP (Figs. 2b and d) were analogical with  
246 those at Beijing station (Fig. 2a). Meanwhile, the simulated AOD at Xianghe (Fig.  
247 2c) was relatively lower than those at other stations; it might be that Xianghe is a  
248 rural station and was less polluted than urban station during this episode.

249 Considering that the available observational AOD data was quite limited, and the  
250 aerosol extinction was mainly attributed to scattering and absorption of solar  
251 radiation by  $\text{PM}_{2.5}$  and their hygroscopic growth with relative humidity (Cheng et al.,  
252 2006), next we compared the simulated  $\text{PM}_{2.5}$  concentrations with corresponding  
253 in-situ observation over the model domain. As shown in Fig. 3, the simulated and  
254 observed pollution were both initiated over Henan province on 6<sup>th</sup>, further  
255 intensified and shifted northward afterwards. The polluted center located over south  
256 of Hebei province and maintained until 10<sup>th</sup>, with the maximum  $\text{PM}_{2.5}$  concentration  
257 exceeding  $440\mu\text{g m}^{-3}$ . The results indicated that WRF-Chem could well capture the  
258 spatial features of  $\text{PM}_{2.5}$  and its temporal variation, in spite of the slight discrepancy  
259 of the center position during 9<sup>th</sup> and 10<sup>th</sup>.

260 To further assess the temporal evolutions of the pollution, the simulated  $\text{PM}_{2.5}$   
261 concentrations at three major cities (Beijing, Shijiazhuang and Tianjin, shown as  
262 black dots in Fig. 1a) in northern China were compared with those observation as  
263 shown in Fig. 4. It showed that the hourly variations of  $\text{PM}_{2.5}$  concentration



264 including the occurrence of several high peaks at the three cities could be reasonably  
265 reproduced by WRF-Chem, despite the slight overestimation (underestimation) of  
266 the peak magnitude during 9<sup>th</sup> to 10<sup>th</sup> at Beijing and Shijiazhuang (Tianjin). The  
267 correlation coefficients (R) between simulation and observation at Beijing,  
268 Shijiazhuang and Tianjin were 0.85, 0.89 and 0.76, respectively.

### 269 **3.2 Aerosol effects on meteorological simulations**

270 In this section, the influences of aerosol-radiation interaction on the spatial and  
271 temporal variations of radiation and energy budget simulated by WRF model were  
272 analyzed, and their impacts on the forecasts of meteorological fields were discussed  
273 further.

#### 274 **3.2.1 Aerosol impacts on simulations of radiative forcing and heat fluxes**

275 To illustrate the impacts of aerosol-radiation interaction on the forecasts of  
276 radiation during the pollution event, the simulated surface downward SW radiation  
277 and net radiation at Beijing, Tianjin, Taiyuan and Jinan, as denoted by the triangles  
278 in Fig. 1a, were compared with observations in Fig. 5. To show the relationship with  
279 aerosol, the time series of AOD for Dec. 3<sup>th</sup> -11<sup>th</sup> were overlay as gray shadings in  
280 Fig. 5. During the clean stage with quite low AOD values (close to 0) before 6<sup>th</sup> Dec.,  
281 both simulations with and without aerosols reasonably reproduced the temporal  
282 variation of downward SW at Beijing despite the slightly overestimation during the  
283 noon-time (Fig. 5a). However, the overestimated downward SW in NoAero turned  
284 to intensify extensively since 6<sup>th</sup> Dec. and sustained till 10<sup>th</sup> Dec., accompanied by



285 the occurrence of the pollution with the high AOD value. Meanwhile, the downward  
286 SW was much lower in Aero than that in NoAero due to aerosol extinction, with  
287 resembled temporal variations and comparable magnitude at the peak time compared  
288 to the observations. Similarly, the variations of downward SW from Aero simulation  
289 were also closer to observations at Tianjin, Taiyuan and Jinan than those in NoAero  
290 (Figs. 5b-d). It was noted that the most significant improvement of simulated  
291 downward SW at Jinan appeared on 10<sup>th</sup> Dec. and was later than that at Beijing,  
292 which was consistent with the AOD's variations at Jinan. Moreover, the surface  
293 energy balance was also affected by the reduction of downward SW radiation  
294 reaching the ground due to the presence of aerosol particles. As shown in Figs. 5e-h,  
295 in corresponding to the changes in downward SW, the variations of net radiation at  
296 surface in Aero were also in better agreement with observation during the polluted  
297 period than in NoAero, particularly during daytime with the high AOD values.

298 To further quantify the influence of the aerosol-radiation interaction on the  
299 diurnal variation of surface radiation, next we compared the simulated averaged  
300 diurnal variation of downward SW and net radiation during the polluted episode (6<sup>th</sup>  
301 to 10<sup>th</sup>) with observation. Figure 6a showed that there existed a large overestimation  
302 of surface downward SW during the daytime in NoAero. Particularly, the  
303 overestimated downward SW tended to increase since morning (0800 LT) and peak  
304 at noon (1300 LT) with the maximum bias reaching  $226.5 \text{ W m}^{-2}$ , and the mean bias  
305 of  $\sim 149.4 \text{ W m}^{-2}$  during daytime (averaged during 0800 to 1800 LT, Table 2).



306 However, the overestimated SW radiation was remarkably reduced in Aero with the  
307 mean bias of  $38.0 \text{ W m}^{-2}$  during daytime. Similarly, the diurnal variation and  
308 magnitude of downward SW radiation at surface were also better captured at Tianjin,  
309 Taiyuan and Jinan in Aero (Figs. 6b–d), with the lower bias ( $70.9 \text{ W m}^{-2}$ ,  $118.3 \text{ W}$   
310  $\text{m}^{-2}$  and  $97.7 \text{ W m}^{-2}$ ) than in NoAero ( $115.5 \text{ W m}^{-2}$ ,  $155.0 \text{ W m}^{-2}$  and  $149.1 \text{ W m}^{-2}$ )  
311 during daytime. Consistent with this finding, the reduction of downward SW was  
312 also reported in United States (Zhang et al., 2010) and Europe (Toll et al., 2016)  
313 with relatively lower decrease ( $10 \text{ W m}^{-2}$  and  $18 \text{ W m}^{-2}$ ); the relatively larger  
314 reductions ( $30\text{--}110 \text{ W m}^{-2}$ ) in northern China is possibly due to the higher aerosol  
315 load. Figures 6e–h presented the diurnal variations of net radiation, with positive  
316 (negative) net radiation during daytime (nighttime) in observation, and the NoAero  
317 tended to overestimate (underestimate) the net radiation at surface during daytime  
318 (nighttime), indicating that there existed surplus energy income and outcome in  
319 model than those in observation, inducing the larger magnitude of diurnal cycle of  
320 net radiation. By including the aerosol-radiation interaction in the model, the  
321 simulated diurnal variations of net radiation were markedly improved, particularly  
322 during daytime with the reduction of bias by 85.3%, 50.0%, 35.4%, and 44.1% at  
323 Beijing, Tianjin, Taiyuan and Jinan, respectively.

324 In response to the decrease of downward SW radiation and net radiation at the  
325 ground during daytime, the surface fluxes also changed in presence of aerosol  
326 extinction within the energy-balanced system. Figure 7 displayed the difference of



327 surface sensible and latent heat flux between Aero and NoAero at 1300LT, when the  
328 influences of the aerosol on radiation reaching the peak. Comparing to the NoAero  
329 simulation, both the surface sensible and latent heat flux emitted by the surface were  
330 reduced in the Aero simulation, with the domain-average of  $16.1 \text{ W m}^{-2}$  (18.5%) and  
331  $6.8 \text{ W m}^{-2}$  (13.4%) respectively. It was noted that the decrease of the surface latent  
332 heat flux was less pronounced than that of surface sensible heat flux, suggesting the  
333 impact of aerosol-radiation interaction on the humidity was less significant than that  
334 of temperature, which was also reported over United States (Fan et al., 2008) and  
335 western Europe (Péré et al., 2011).

### 336 **3.2.2 Aerosol impacts on simulations of temperature, PBLH and wind fields**

337 The changes in radiation and energy budget through the impacts of  
338 aerosol-radiation interaction would certainly induce the changes in PBL  
339 thermodynamics and dynamics, which would result in changes in the forecasts of  
340 meteorological fields. The impacts on the forecasts of 2-m temperature, PBLH and  
341 wind fields due to the aerosol-radiation interaction were discussed in the following  
342 subsection.

343 Figure 8 presented the diurnal variation of averaged bias of 2-m temperature  
344 during polluted period in NoAero (upper panel) and Aero (lower panel) compared  
345 with the in-situ observation during 1100 LT to 2300 LT. It was obvious that the  
346 temperature of NoAero was significantly overestimated for a wide range over  
347 northern China, particularly over the plain areas including south of Hebei, Henan



348 and Shanxi provinces. The warm biases tended to intensify in the afternoon and  
349 reach  $\sim 3^{\circ}\text{C}$  over south part of Hebei province (Figs. 8b–c). Accompanied by the  
350 warm biases over plain areas throughout the day, the mountain areas were  
351 dominated by the cold biases until 1700 LT, and turned to be warm biases afterwards,  
352 which were attributed by the frozen water in soil due to wet bias of soil moisture  
353 over mountain areas, inducing overestimated energy transport from atmosphere to  
354 soil during daytime. Compared to NoAero, the lower temperature in Aero due to the  
355 decreased surface solar radiation, caused by aerosol extinction led to the reduced  
356 warm bias in NCP region. However, the cold bias in Beijing area was slightly  
357 intensified, which may partly relevant with the overestimated  $\text{PM}_{2.5}$  concentration in  
358 Beijing and can be improved by incorporating more accurate aerosol information in  
359 the future. It was noted that the cold biases over mountain areas associated with the  
360 model physics deficiency can not be corrected by aerosol-radiation effects, thus the  
361 correction of aerosol-radiation effect may get complex results and differ with  
362 regions due to the model pre-existing deficiencies.

363 To quantitatively evaluate the agreement of simulated 2-m temperature with  
364 observations, the mean bias and root mean square error (RMSE) were employed,  
365 and their diurnal variations during the polluted episode averaged over NCP, denoted  
366 by the purple box in Fig. 1a, were displayed in Fig. 9. As shown in Fig. 9a, the warm  
367 bias in NoAero sustained during the entire 24-hr forecast, ranging from  $0.3^{\circ}\text{C}$  to  
368  $0.9^{\circ}\text{C}$ . Compared to NoAero, the NCP area-averaged warm bias was remarkably



369 reduced by  $\sim 0.40^{\circ}\text{C}$  ( $\sim 73.9\%$ ) due to aerosol-radiation interaction, with the  
370 maximum reaching  $\sim 0.54^{\circ}\text{C}$  ( $\sim 95.0\%$ ) at 1100 LT (Figs. 9a and c). Consistently  
371 with mean bias, the RMSE was also lower in Aero than NoAero, particularly during  
372 1100 to 2000 LT during the daytime (Figs. 9b and d).

373 The aerosol-radiation interaction may also have profound impacts on atmospheric  
374 structure in addition to radiation and temperature (Rémy et al., 2015). PBLH is one  
375 of the key parameters to describe the structure of PBL and closely related to air  
376 pollution. It was indicated that the mean daytime PBLH over northern China were  
377 around 300–600m (Fig. 10a), and declined generally 40–200m (10%–40%) in Aero  
378 over the region with highest  $\text{PM}_{2.5}$  concentration, particularly over Beijing, Tianjin  
379 and Hebei (Figs. 10b–c). As shown in dashed lines in Fig. 11, the NCP  
380 area-averaged PBLH at noon-time (1400 LT) was diminished dramatically by  
381 aerosol-radiation interaction during the pollution event over northern China, with the  
382 maximum decrease reaching  $-155.2\text{m}$  on 7<sup>th</sup> Dec. The reduction of PBLH could be  
383 the consequence of more stable atmosphere in Aero than NoAero, which was  
384 induced by the terrestrial cooling in the lower part of the planetary boundary layer  
385 and the solar heat due to the absorbing in the upper layers (solid lines in Fig. 11).

386 The near surface wind fields changes due to aerosol-radiation interaction were  
387 further investigated. Figure 12 shows the wind vector in NoAero (upper panel), Aero  
388 (middle panel) and their difference (lower panel). It can be seen from Fig. 12a-e that  
389 the northern China was dominated by the anticyclonic circulation, accompanied by



390 the relatively weaker northeast wind over Beijing and Hebei areas. The comparisons  
391 of Aero and NoAero (Figs. 12 k-o) shown that the northeast wind was increased  
392 with the maximum reaching  $1 \text{ m s}^{-1}$  by aerosol-radiation interaction over Beijing  
393 and Hebei, where high particles concentration located (shadings in Figs. 12 f-j).  
394 Figures 12k-o also indicated the changes of west wind over the south part of the  
395 domain and southeast wind over the ocean areas, which tended to weaken the  
396 anticyclonic circulation and thus declined the wind speed there. The reduced wind  
397 speed due the inclusion of aerosol-radiation interaction was possible due to the  
398 thermal-wind adjustment in response to the more stable near-surface atmosphere,  
399 which was also addressed in previous work using WRF-Chem (Zhang et al., 2015).

400 The comparisons between simulated wind speeds against in-situ observation  
401 averaged during 6<sup>th</sup> to 10<sup>th</sup> Dec. were displayed in Fig. 13. In regard of NoAero, the  
402 simulated wind speed at 10m was overestimated over the nearly whole domain with  
403 the maximum bias up to  $3 \text{ m s}^{-1}$  except some mountain sites (upper and middle  
404 panels in Fig.13). It might be due to the omission of UCM model as the  
405 overestimation is more prominent in city clusters (especially in Beijing and southern  
406 Hebei) than other areas. Figures 13k-o showed the difference of absolute value of  
407 bias between Aero and NoAero and indicated the bias of simulated wind speed were  
408 decreased over south and northeast part of the domain during afternoon (Figs. 13k-m)  
409 by aerosol-radiation interaction, while were increased over Beijing and Hebei area  
410 particularly during nightfall (Fig. 13n) due to the intensified wind speed there. The



411 NCP area-averaged bias and RMSE of wind speed at 10m were further shown in  
412 Figure 14. It was seen that the aerosol-radiation interaction helped to reduce the  
413 overestimation of wind speed at 10m up to  $0.08 \text{ m s}^{-1}$  (~7.8%), particular during  
414 daytime (Figs. 14a and c). Correspondingly, the RMSE of Aero was also lower than  
415 that of NoAero, indicating that the inclusion of aerosol-radiation interaction helped  
416 to improve the prediction of near surface wind speed on the domain-averaged scale.

417 Although the changes of wind speed is less straightforward than that of radiation,  
418 the aerosol-radiation interactions can also affect dynamic fields (vertical wind shear)  
419 through the changes of atmospheric thermal structure and the thermal wind relation  
420 when the interaction lasts long enough (Huang et al., 2019). Figure 15 displayed  
421 vertical profiles of wind speed at the stations of Beijing and Xingtai in simulation  
422 and verified with sounding observations. It was shown that the NoAero  
423 underestimated (overestimated) the low levels wind speed at 0800 LT (2000 LT) at  
424 both Beijing and Xingtai. However, the wind speed were increased (decreased) at  
425 0800 LT (2000 LT) in Aero relative to NoAero, indicating the positive impacts on  
426 the simulation of atmospheric winds by aerosol-radiation interaction.

427 Since the forecast meteorological fields by WRF (RMPAS-ST) is routinely  
428 applied to WRF-Chem (RMAPS-Chem) as meteorological ICs in the air quality  
429 operational system at IUM, the changed meteorology due to aerosol-radiation  
430 interaction will further influence the forecast of pollution through meteorological  
431 ICs. In regard of further feedback of aerosol-radiation interactions to the transport



432 and dissipation of the pollutants, their impacts on wind field at 850hPa were further  
433 discussed as it is strongly correlated with haze formation (Zhang et al., 2018; Zhai et  
434 al., 2019). Figures 16 a-e display that northern China was dominated by the  
435 anticyclone circulation at 850hPa, associated with the southwest (northwest) wind in  
436 the west (east) of the northern part of the domain. The difference of U (zonal,  
437 eastward is positive) winds between Aero and NoAero (middle panel in Fig. 16)  
438 showed that the U wind was intensified over west Hebei, accompanied by the quite  
439 small changes in Beijing area, indicating that the increased U wind was blocked by  
440 the mountains and could not transport the pollutants over Hebei and Beijing to the  
441 east (Figs. 16 f-h). On the other hand, the changes of V (meridional, northward is  
442 positive) show different patterns over north and south of the 38° N (lower panel in  
443 Fig. 16). In the south part, the increased northward wind due to aerosol-radiation  
444 interaction may help to transport pollutants from highly polluted areas to Hebei and  
445 Beijing. In the north of the domain, the negative (positive) changes of V wind  
446 indicated the reduced northward (southward) wind in west (east) of Hebei, which  
447 could suppress the diffusion of the pollutants. As a result, both U and V changes  
448 induced by the aerosol-radiation interaction will prevent pollutants from dispersing  
449 and may exacerbate the pollution in Hebei and Beijing, which confirms the more  
450 stable boundary layer due to aerosol-radiation interaction as discussed earlier.

#### 451 **4. Concluding remarks**

452 To facilitate the future inclusion of aerosol-radiation interactions in the regional



453 operational NWP system – RMAPS-ST (adapted from WRF) at IUM, CMA, the  
454 impacts of aerosol-radiation interactions on the forecast of surface radiation and  
455 meteorological parameters during a heavy pollution event (Dec. 6<sup>th</sup> -10<sup>th</sup>, 2015) over  
456 northern China were investigated. The aerosol information (550-nm AOD 2D field)  
457 were simulated by WRF-Chem and then offline-coupled into RRTMG radiation  
458 scheme of WRF to enable the aerosol-radiation feedback in the forecast. Two sets of  
459 24-hour forecasts were performed at 00UTC from Dec. 2<sup>nd</sup>-11<sup>th</sup>, 2015. The only  
460 difference between the two sets of forecasts was whether the aerosol radiative  
461 feedback was activated (Aero) or not (NoAero), while the other schemes remained  
462 the same.

463 The capability of WRF-chem to reproduce the polluted episode was confirmed  
464 first before the offline-coupling of AOD to WRF. The results indicated that the  
465 temporal variations of simulated AOD at 550nm was in consistent with AERONET  
466 and in-situ observation at IAP. Furthermore, the spatial distributions of PM<sub>2.5</sub> as well  
467 as their magnitude, particularly during the peak stage (8<sup>th</sup> to 9<sup>th</sup>) of the pollution  
468 event were reasonably captured by WRF-Chem, with the correlation coefficients of  
469 0.85, 0.89 and 0.76 at Beijing, Shijiazhuang and Tianjin, respectively.

470 Further, the impacts of aerosols-radiation interaction on the forecasts of surface  
471 radiation, energy budget, and meteorology parameters were evaluated against  
472 surface and sounding observations. The results showed that the decrease of  
473 downward SW radiation reaching surface induced by aerosol effects helped to



474 reduce the overestimation of SW radiation during daytime. Moreover, the simulated  
475 surface radiation budget has also been improved, with the biases of net radiation at  
476 surface decreased by 85.3%, 50.0%, 35.4%, and 44.1% during daytime at Beijing,  
477 Tianjin, Taiyuan and Jinan respectively, accompanied by the reduction of sensible  
478 ( $16.1 \text{ W m}^{-2}$ , 18.5%) and latent ( $6.8 \text{ W m}^{-2}$ , 13.4%) heat fluxes emitted by the  
479 surface at noon-time.

480 The energy budget changed by aerosol extinction further cools 2-m temperature  
481 by  $\sim 0.40^\circ\text{C}$  over NCP, reducing warm bias by  $\sim 73.9\%$  and also leading to lower  
482 RMSE, particularly during daytime. Since aerosol cools the lower planetary  
483 boundary layer and meanwhile warms the high atmosphere, it induced the more  
484 stable stratification of the atmosphere and the declination of PBLH by 40–200m  
485 (10%–40%) over NCP. Associating with the changes of planetary boundary structure  
486 and more stable near-surface atmosphere, the aerosol-radiation interaction tended to  
487 weaken the anticyclonic circulation including the east wind over the south part of  
488 the domain and northwest wind over the ocean areas. Thus the bias of wind speed  
489 over south and northeast part of the domain were decreased particularly during the  
490 afternoon, while increased over Beijing and Hebei area. In regard of NCP-average,  
491 the overestimated 10m wind speed was improved during whole day with the  
492 maximum up to  $0.08 \text{ m s}^{-1}$  ( $\sim 7.8\%$ ) at 1400LT. The comparison between simulated  
493 vertical profiles of atmospheric wind speed with soundings also indicated that Aero  
494 was in better agreement with observation and aerosol-radiation interaction helped to



495 improve the prediction of dynamic fields such as atmospheric wind through the  
496 thermal wind relation by altering the atmospheric structure.

497 The impacts of aerosol-radiation interactions on wind field at 850hPa were  
498 further discussed. The results showed that aerosol-radiation interaction will prevent  
499 pollutants from dispersing and may exacerbate the pollution through changes of both  
500 U and V wind, which confirms the more stable boundary layer due to  
501 aerosol-radiation. These wind field changes may also influence the forecast of the  
502 transport and dissipation of the pollutants by WRF-Chem through changed  
503 meteorological ICs.

504 This study analyzed the impacts of aerosol-radiation interaction on radiation and  
505 meteorological forecast by using the offline-coupling of WRF and high-frequent  
506 updated AOD simulated by WRF-Chem, which is more computationally economic  
507 than the online simulation with the integration time for 96h forecast of about 40% of  
508 that for online simulation. This approach allows for a potential application to include  
509 aerosol-radiation interaction in our current operational NWP systems. The results  
510 revealed that aerosol-radiation interaction had profound influence on the  
511 improvement of predictive accuracy and the potential prospects for its application in  
512 regional NWP in northern China. Given that most of these analyses were based on a  
513 single case of pollution occurred during the wintertime of 2015, there is clearly a  
514 need for further research on more polluted cases to achieve more quantitative results  
515 before the operational application. As the simulated AOD was adopted in the present



516 study, it should be noted that there exists a discrepancy between simulated AOD and  
517 observation in both spatial distribution and temporal variation, which may influence  
518 the impacts of aerosol-radiation interaction. Meanwhile, surface energy budget and  
519 atmospheric dynamics are also influenced by aerosol-cloud interaction, which are  
520 related to cloud microphysical processes and are not discussed in this study.

521

522 **Author contribution** Yang Yang, Xiujuan Zhao and Dan Chen designed the  
523 experiments and Yang Yang performed the simulations and carried them out. Yang  
524 Yang prepared the manuscript with contributions from all co-authors.

525

526 **Acknowledgments** This work was jointly supported by the National Key R&D  
527 Program of China (grant nos. 2017YFC1501406 and 2018YFF0300102), Natural  
528 Science Foundation of Beijing Municipality (8161004), the National Natural Science  
529 Foundation of China (grant nos. 41705076, 41705087 and 41705135) and  
530 Beijing Major Science and Technology Project (Z181100005418014).



531 **Reference**

532 Ackerman, A. S., Toon, O. B., Stevens, D. E., Heymsfield, A. J., Ramanathan, V.,  
533 and Welton, E. J.: Reduction of tropical cloudiness by soot, *Science*, 288, 1042–  
534 1047, <https://doi.org/10.1126/science.288.5468.1042>, 2000.

535 Baklanov, A., Schlünzen, K., Suppan, P., Baldasano, J., Brunner, D., Aksoyoglu, S.,  
536 Carmichael, G., Douros, J., Flemming, J., Forkel, R., Galmarini, S., Gauss, M.,  
537 Grell, G., Hirtl, M., Joffre, S., Jorba, O., Kaas, E., Kaasik, M., Kallos, G., Kong,  
538 X., Korsholm, U., Kurganskiy, A., Kushta, J., Lohmann, U., Mahura, A.,  
539 Manders-Groot, A., Maurizi, A., Moussiopoulos, N., Rao, S. T., Savage, N.,  
540 Seigneur, C., Sokhi, R. S., Solazzo, E., Solomos, S., Sørensen, B., Tsegas, G.,  
541 Vignati, E., Vogel, B., and Zhang, Y.: Online coupled regional meteorology  
542 chemistry models in Europe: current status and prospects, *Atmos. Chem. Phys.*,  
543 14, 317–398, <https://doi.org/10.5194/acp-14-317-2014>, 2014.

544 Chan, C. K. and Yao, X.: Air pollution in mega cities in China, *Atmos. Environ.*, 42,  
545 1–42, <https://doi.org/10.1016/j.atmosenv.2007.09.003>, 2008.

546 Chen, D., Liu, Z., Davis, C., and Gu, Y.: Dust radiative effects on atmospheric  
547 thermodynamics and tropical cyclogenesis over the Atlantic Ocean using  
548 WRF-Chem coupled with an AOD data assimilation system, *Atmos. Chem. Phys.*,  
549 17, 7917–7939, <https://doi.org/10.5194/acp-17-7917-2017>, 2017.

550 Chen, F. and Dudhia, J.: Coupling an advanced land surface-hydrology model with  
551 the Penn State-NCAR MM5 modeling system. Part I: Model implementation and



552 sensitivity, *Mon. Wea. Rev.*, 129, 569–585, doi:  
553 10.1175/1520-0493(2001)129<0569:CAALSH>2.0.CO;2, 2001.

554 Cheng, X., Sun, Z., Li, D., Xu, X., Jia, M., and Cheng, S.: Short-term aerosol  
555 radiative effects and their regional difference during heavy haze episodes in  
556 January 2013 in China, *Atmos. Environ.*, 165, 248–263,  
557 <http://dx.doi.org/10.1016/j.atmosenv.2017.06.040>, 2017.

558 Cheng, Y. F., Eichler, H., Wiedensohler, A., Heintzenberg, J., Zhang, Y. H., Hu, M.,  
559 Herrmann, H., Zeng, L.M., Liu, S., Gnauk, T., Brüggemann, E., and He, L.Y.,  
560 Mixing state of elemental carbon and non-light-absorbing aerosol components  
561 derived from in situ particle optical properties at Xinken in Pearl River Delta of  
562 China, *J. Geophys. Res.-Atmos.*, 111, D20204, doi: 10.1029/2005JD006929,  
563 2006.

564 Chou, M. D. and Suarez, M. J.: A solar radiation parameterization for atmospheric  
565 studies, *Tech. Rep. NASA/TM-1999-104606*, 15, Technical Report Series on  
566 Global Modeling and Data Assimilation NASA, 1999.

567 Ek, M. B., Mitchell, K. E., Lin, Y., Rogers, E., Grunmann, P., Koren, V., Gayno, G.,  
568 and Tarpley, J.D.: Implementation of Noah land surface model advances in the  
569 National Centers for Environmental Prediction operational mesoscale Eta model,  
570 *J. Geophys. Res.-Atmos.*, 108, 8851, doi:10.1029/2002JD003296, 2003.

571 Elser, M., Huang, R.-J., Wolf, R., Slowik, J. G., Wang, Q., Canonaco, F., Li, G.,  
572 Bozzetti, C., Daellenbach, K. R., Huang, Y., Zhang, R., Li, Z., Cao, J.,



- 573 Baltensperger, U., El-Haddad, I., and Prévôt, A. S. H.: New insights into PM<sub>2.5</sub>  
574 chemical composition and sources in two major cities in China during extreme  
575 haze events using aerosol mass spectrometry, *Atmos. Chem. Phys.*, 16, 3207–  
576 3225, <https://doi.org/10.5194/acp-16-3207-2016>, 2016.
- 577 Fan, J., Zhang, R., Tao, W. K., and Mhor, K. I.: Effects of aerosol optical properties  
578 on deep convective clouds and radiative forcing, *J. Geophys. Res.*, 113, D08209,  
579 doi:10.1029/2007JD009257, 2008.
- 580 Ghan, S. J., Liu, X., Easter, R. C., Zaveri, R., Rasch, P. J., Yoon, J.-H., Eaton, B.:  
581 Toward a Minimal Representation of Aerosols in Climate Models: Comparative  
582 Decomposition of Aerosol Direct, Semidirect, and Indirect Radiative Forcing, *J.*  
583 *Clim.*, 2012, 25, 6461–6476, doi: 10.1175/JCLI-D-11-00650.1, 2012.
- 584 Grell, G. A. and Baklanov, A.: Integrated modelling for forecasting weather and air  
585 quality: a call for fully coupled approaches, *Atmos. Environ.*, 45, 6845–6851,  
586 <https://doi.org/10.1016/j.atmosenv.2011.01.017>, 2011.
- 587 Grell, G. A. and Dévényi, D.: A generalized approach to parameterizing convection  
588 combining ensemble and data assimilation techniques, *Geophys. Res. Lett.*, 29,  
589 1693, doi: 10.1029/2002GL015311, 2002.
- 590 Grell, G., Freitas, S. R., Stuefer, M., and Fast, J.: Inclusion of biomass burning in  
591 WRF-Chem: impact of wildfires on weather forecasts, *Atmos. Chem. Phys.*, 11,  
592 5289–5303, <https://doi.org/10.5194/acp-11-5289-2011>, 2011.
- 593 Guo, J., Deng, M., Lee, S. S., Wang, F., Li, Z., Zhai, P., Liu, H., Lv, W., Yao, W., and



- 594 Li, X.: Delaying precipitation and lightning by air pollution over the pearl river  
595 delta. Part I: observational analyses, *J. Geophys. Res.-Atmos*, 121, 6472–6488,  
596 doi:10.1002/2015JD023257, 2016.
- 597 Hansen, J., Sato, M., and Ruedy, R.: Radiative forcing and climate response, *J.*  
598 *Geophys. Res.-Atmos*, 102, 6831–6864, <https://doi.org/10.1029/96JD03436>,  
599 1997.
- 600 Hong, S.-Y., Noh, Y., and Dudhia, J.: A new vertical diffusion package with an  
601 explicit treatment of entrainment processes, *Mon. Weather Rev.*, 134, 2318–2341,  
602 doi:10.1175/Mwr3199.1, 2006.
- 603 Huang, C.-C., Chen, S.-H., Lin, Y.-C., Earl, K., Matsui, T., Lee, H.-H., Tsai, I.-C.,  
604 Chen, J.-P., and Cheng, C.-T.: Impacts of Dust–Radiation versus Dust–Cloud  
605 Interactions on the Development of a Modeled Mesoscale Convective System  
606 over North Africa, *Mon. Weather Rev.*, 47, 3301–3326.  
607 <https://doi.org/10.1175/MWR-D-18-0459.1>, 2019.
- 608 Huang, X., Ding, A., Liu, L., Liu, Q., Ding, K., Niu, X., Nie, W., Xu, Z., Chi, X.,  
609 Wang, M., Sun, J., Guo, W., and Fu, C.: Effects of aerosol–radiation interaction  
610 on precipitation during biomass-burning season in East China, *Atmos. Chem.*  
611 *Phys.*, 16, 10063 – 10082, <https://doi.org/10.5194/acp-16-10063-2016>, 2016.
- 612 Iacono, M. J., Delamere, J. S., Mlawer, E. J., Shephard, M. W., Clough, S. A.,  
613 Collins, W. D.: Radiative forcing by long-lived greenhouse gases: Calculations  
614 with the AER radiative transfer models, *J. Geophys. Res.-Atmos*, 113, D13, doi:



- 615 10.1029/2008JD009944, 2008.
- 616 Kain, J. S.: The Kain-Fritsch convective parameterization: An update, *J. Appl.*  
617 *Meteorol.*, 43, 170–181, 2004.
- 618 Kaufman, Y. J., Tanre, D., and Boucher, O.: A satellite view of aerosols in the  
619 climate system, *Nature*, 419, 215–223, <http://dx.doi.org/10.1038/nature01091>,  
620 2002.
- 621 Liao, H., Chen, W. T., and Seinfeld, J. H.: Role of climate change in global  
622 predictions of future tropospheric ozone and aerosols, *J. Geophys. Res.*, 111,  
623 D12304, doi:10.1029/2005JD006852, 2006.
- 624 Liao, L., Lou, S. J., Fu, Y., Chang, W. J., and Liao, H.: Radiative forcing of aerosols  
625 and its impact on surface air temperature on the synoptic scale in eastern China,  
626 *Chinese J. Atmos. Sci.* (in Chinese), 39, 68–82, doi: doi:  
627 10.3878/j.issn.1006-9895.1402.13302, 2015.
- 628 Liu, X., Zhang, Y., Cheng, Y., Hu, M., and Han, T.: Aerosol hygroscopicity and its  
629 impact on atmospheric visibility and radiative forcing in Guangzhou during the  
630 2006 PRIDE-PRD campaign, *Atmos. Environ.* 60, 59–67,  
631 <https://doi.org/10.1016/j.atmosenv.2012.06.016>, 2012.
- 632 Mlawer, E. J., Taubman, S. J., Brown, P. D., Iacono, M. J. and Clough, S. A.:  
633 Radiative transfer for inhomogeneous atmospheres: RRTM, a validated  
634 correlated-k model for the longwave, *J. Geophys. Res.*, 102,  
635 doi:10.1029/97JD00237. 16663–16682, 1997.



- 636 Mulcahy, J. P., Walters, D. N., Bellouin, N., and Milton, S. F.: Impacts of increasing  
637 the aerosol complexity in the Met Office global numerical weather prediction  
638 model, *Atmos. Chem. Phys.*, 14, 4749–4778,  
639 <https://doi.org/10.5194/acp-14-4749-2014>, 2014.
- 640 Oreopoulos, L., Mlawer, E., Delamere, J., Shippert, T., Cole, J., Fomin, B., Iacono,  
641 M., Jin, Z., Li, J., Manners, J., Räisänen, P., Rose, F., Zhang, Y., Wilson, M. J.,  
642 and Rossow, W. B.: The Continual Intercomparison of Radiation Codes: Results  
643 from Phase I, *J. Geophys. Res.-Atmos.*, 117, D06118,  
644 <https://doi.org/10.1029/2011JD016821>, 2012.
- 645 Péré, J. C., Mallet, M., Pont, V., and Bessagnet B.: Impact of aerosol direct radiative  
646 forcing on the radiative budget, surface heat fluxes, and atmospheric dynamics  
647 during the heat wave of summer 2003 over western Europe: A modeling study, *J.*  
648 *Geophys. Res.*, 116, D23119, <https://doi.org/10.1029/2011JD016240>, 2011.
- 649 Pleim, J. E.: A Combined local and nonlocal closure model for the atmospheric  
650 boundary layer. Part I: Model description and testing, *J. Appl. Meteorol. Climat.*,  
651 46, 1383–1395, doi: 10.1175/JAM2539.1, 2007.
- 652 Quan, J., Tie, X., Zhang, Q., Liu, Q., Li, X., Gao, Y., and Zhao D.: (2014).  
653 Characteristics of heavy aerosol pollution during the 2012–2013 winter in Beijing,  
654 China, *Atmos. Environ.*, 88, 83–89,  
655 <https://doi.org/10.1016/j.atmosenv.2014.01.058>, 2014.
- 656 Ramanathan, V., Crutzen, P. J., Kiehl, J. T., and Rosenfeld, D.: Aerosols, Climate



- 657 and the Hydrological Cycle, *Science*, 294, 2119–2124, 2001.
- 658 Rémy, S., Benedetti, A., Bozzo, A., Haiden, T., Jones, L., Razinger, M., Flemming,  
659 J., Engelen, R. J., Peuch, V. H., and Thepaut, J. N.: Feedbacks of dust and  
660 boundary layer meteorology during a dust storm in the eastern Mediterranean,  
661 *Atmos. Chem. Phys.*, 15, 12909–12933,  
662 <https://doi.org/10.5194/acp-15-12909-2015>, 2015.
- 663 Rodwell, M. J. and Jung T.: Understanding the local and global impacts of model  
664 physics changes: an aerosol example, *Q. J. Roy. Meteor. Soc.*, 134, 1479–1497,  
665 <https://doi.org/10.1002/qj.298>, 2008.
- 666 Rogers, R. E., Deng, A. J., Stauffer, D. R., Gaudet, B. J., Jia, Y. Q., Soong, S. T., and  
667 Tanrikulu, S.: Application of the Weather Research and Forecasting Model for Air  
668 Quality Modeling in the San Francisco Bay Area, *J. Appl. Meteor. Clim.*, 52,  
669 1953–1973, doi: 10.1175/JAMC-D-12-0280.1, 2013.
- 670 Ruiz-Arias, J. A., Dudhia, J., and Gueymard, C. A.: A simple parameterization of the  
671 short-wave aerosol optical properties for surface direct and diffuse irradiances  
672 assessment in a numerical weather model, *Geosci. Model Dev.*, 7, 1159–1174,  
673 doi:10.5194/gmd-7-1159-2014, 2014.
- 674 Sekiguchi, A., Shimadera, H., and Kondo, A.: 2018, Impact of Aerosol Direct Effect  
675 on Wintertime PM<sub>2.5</sub> Simulated by an Online Coupled Meteorology-Air Quality  
676 Model over East Asia, *Aerosol and Air Quality Research*, 18: 1068–1079, doi:  
677 10.4209/aaqr.2016.06.0282, 2018.



- 678 Thompson, G., Field, P. R., Rasmussen, R. M., and Hall, W. D.: Explicit forecasts of  
679 winter precipitation using an improved bulk microphysics scheme. Part II:  
680 Implementation of a new snow parameterization, *Mon. Weather Rev.*, 136, 5095–  
681 5115, <https://doi.org/10.1175/2008MWR2387.1>, 2008.
- 682 Toll, V., Gleeson, E., Nielsen, K.P., Männik, A., Mašek, J., Rontu, L., and Post, P.:  
683 Impacts of the direct radiative effect of aerosols in numerical weather prediction  
684 over Europe using the ALADIN-HIRLAM NWP system, *Atmos. Res.*, 172-173,  
685 163-173, <https://doi.org/10.1016/j.atmosres.2016.01.003>, 2016.
- 686 Toll, V., Reis, K., Ots, R., Kaasik, M., Männik, A., Prank, M., Sofiev, M.: SILAM  
687 and MACC reanalysis aerosol data used for simulating the aerosol direct radiative  
688 effect with the NWP model HARMONIE for summer 2010 wildfire case in  
689 Russia, *Atmos. Environ.*, 121, 75-85,  
690 <https://doi.org/10.1016/j.atmosenv.2015.06.007>, 2015.
- 691 Wang, H., Shi, G. Y., Zhang, X. Y., Gong, S. L., Tan, S. C., Chen, B., Che, H. Z., and  
692 Li, T.: Mesoscale modelling study of the interactions between aerosols and PBL  
693 meteorology during a haze episode in China Jing–Jin–Ji and its near surrounding  
694 region – Part 2: Aerosols' radiative feedback effects, *Atmos. Chem. Phys.*, 15,  
695 3277-3287, <https://doi.org/10.5194/acp-15-3277-2015>, 2015b.
- 696 Wang, H., Xue, M., Zhang, X. Y., Liu, H. L., Zhou, C. H., Tan, S. C., Che, H. Z.,  
697 Chen, B., and Li, T.: Mesoscale modeling study of the interactions between  
698 aerosols and PBL meteorology during a haze episode in Jing–Jin–Ji (China) and



699 its nearby surrounding region – Part 1: Aerosol distributions and meteorological  
700 features, *Atmos. Chem. Phys.*, 15, 3257–3275,  
701 <https://doi.org/10.5194/acp-15-3257-2015>, 2015a.

702 Wang, J., Wang, S., Jiang, J., Ding, A., Zheng, M., Zhao, B., Wong, D. C., Zhou, W.,  
703 Zheng, G., Wang, L., Pleim, J. E. and Hao, J.: Impact of aerosol–meteorology  
704 interactions on fine particle pollution during China's severe haze episode in  
705 January 2013, *Environ. Res. Lett.*, 9, 094002, doi:10.1088/1748-9326/9/9/094002,  
706 2014.

707 Wang, X., He, X., Miao, S., Dou, Y.: Numerical simulation of the influence of  
708 aerosol radiation effect on urban boundary layer, *Sci. China Earth Sci.*, 61, 1844–  
709 1858, <https://doi.org/10.1007/s11430-018-9260-0>, 2018.

710 Yang, X., Zhao, C., Zhou, L., Wang, Y., Liu, X.: Distinct impact of different types of  
711 aerosols on surface solar radiation in China, *J. Geophys. Res.-Atmos.*, 121,  
712 6459–6471, doi: 10.1002/2016JD024938, 2017b.

713 Yang, Y. and Ren, R. C.: On the contrasting decadal changes of diurnal surface  
714 temperature range between the Tibetan Plateau and southeastern China during the  
715 1980s–2000s, *Adv. Atmos. Sci.*, 34, 181–198, doi: 10.1007/s00376-016-6077-z,  
716 2017a.

717 Yu, H., Kaufman, Y. J., Chin, M., Feingold, G., Remer, L. A., Anderson, T. L.,  
718 Balkanski, Y., Bellouin, N., Boucher, O., Christopher, S., DeCola, P., Kahn, R.,  
719 Koch, D., Loeb, N., Reddy, M. S., Schulz, M., Takemura, T., and Zhou, M.: A



720 review of measurement-based assessments of the aerosol direct radiative effect  
721 and forcing, *Atmos. Chem. Phys.*, 6, 613-666,  
722 <https://doi.org/10.5194/acp-6-613-2006>, 2006.

723 Zaveri, R. A. and Peters, L. K.: A new lumped structure photochemical mechanism  
724 for large-scale applications, *J. Geophys. Res.*, 104, 30387–30415,  
725 <https://doi.org/10.1029/1999JD900876>, 1999.

726 Zhai, S., Jacob, D. J., Wang, X., Shen, L., Li, K., Zhang, Y., Gui, K., Zhao, T., and  
727 Liao, H.: Fine particulate matter (PM<sub>2.5</sub>) trends in China, 2013–2018: separating  
728 contributions from anthropogenic emissions and meteorology, *Atmos. Chem.*  
729 *Phys.*, 19, 11031-11041, <https://doi.org/10.5194/acp-19-11031-2019>, 2019.

730 Zhang, B., Wang, Y., and Hao, J.: Simulating aerosol–radiation–cloud feedbacks on  
731 meteorology and air quality over eastern China under severe haze conditions in  
732 winter, *Atmos. Chem. Phys.*, 15, 2387-2404,  
733 <https://doi.org/10.5194/acp-15-2387-2015>, 2015.

734 Zhang, Q., Ma, Q., Zhao, B., Liu, X., Wang, Y., Jia, B., and Zhang, X.: Winter haze  
735 over North China Plain from 2009 to 2016: Influence of emission and  
736 meteorology, *Environ. Pollut.*, 242, 1308–1318.  
737 [doi:10.1016/j.envpol.2018.08.019](https://doi.org/10.1016/j.envpol.2018.08.019), 2018.

738 Zhang, Q., Quan, J., Tie, X., Li, X., Liu, Q., Gao, Y., and Zhao, D. L.: Effects of  
739 meteorology and secondary particle formation on visibility during heavy haze  
740 events in Beijing, China, *Sci. Total Environ.*, 502, 578–584,



- 741 <https://doi.org/10.1016/j.scitotenv.2014.09.079>, 2015.
- 742 Zhang, Y., Wen, X.-Y., and Jang, C.-J.: Simulating  
743 chemistry-aerosol-cloud-radiation-climate feedbacks over the continental U.S.  
744 using the online-coupled Weather Research Forecasting Model with chemistry  
745 (WRF/Chem), *Atmos. Environ.* 44, 3568–3582,  
746 <https://doi.org/10.1016/j.atmosenv.2010.05.056>, 2010.
- 747 Zhang, Y.-Z., Miao, S.-G., Dai, Y.-J., Liu, Y.-H., Numerical simulation of  
748 characteristics of summer clear day boundary layer in Beijing and the impact of  
749 urban underlying surface on sea breeze (in Chinese), *Chin J. Geophys.* 56,  
750 2558–2573, 2013.
- 751 Zhao, X., Li, Z., Xu, J.: Modification and performance tests of visibility  
752 parameterizations for haze days, *Environ. Sci.*, 40, 1688-1696 (in Chinese), 2019.
- 753 Zheng, Y., Che, H., Xia, X., Wang, Y., Wang, H., Wu, Y., Tao, J., Zhao, H., An, J.,  
754 Li, L., Gui, K., Sun, T., Li, X., Sheng, Z., Liu, C., Yang, X., Liang, Y., Zhang, L.,  
755 Liu, C., Kuang, X., Luo, S., You, Y., and Zhang, X.: Five-year observation of  
756 aerosol optical properties and its radiative effects to planetary boundary layer  
757 during air pollution episodes in North China: Intercomparison of a plain site and  
758 a mountainous site in Beijing, *Sci. Total Environ.*, 674, 140–158.  
759 <https://doi.org/10.1016/j.scitotenv.2019.03.418>, 2019.



760 Table 1. The variables, sources, numbers of sites in the domain/NCP and the  
 761 frequency of chemical and meteorological observations.

Variables	Source of observation	Numbers of sites over the domain/NCP	Frequency	locations
AOD	AERONET	3/3	hourly	black dots in Fig. 1b
AOD	IAP station	1/1	hourly	blue dot in Fig. 1b
PM <sub>2.5</sub>	China National Environmental Monitoring Centre	813/332	hourly	dots in Fig. 3a
radiation	China Meteorological Administration	4/4	hourly	triangles in Fig. 1a
radiation	IAP station	1/1	hourly	triangles in Fig. 1a
2-m temperature	China Meteorological Administration	1157/534	hourly	dots in Fig. 8a
wind at 10m	China Meteorological Administration	1157/534	hourly	dots in Fig. 8a
atmospheric wind	China Meteorological Administration	2/2	0800LT, 2000LT	circles in Fig. 1a

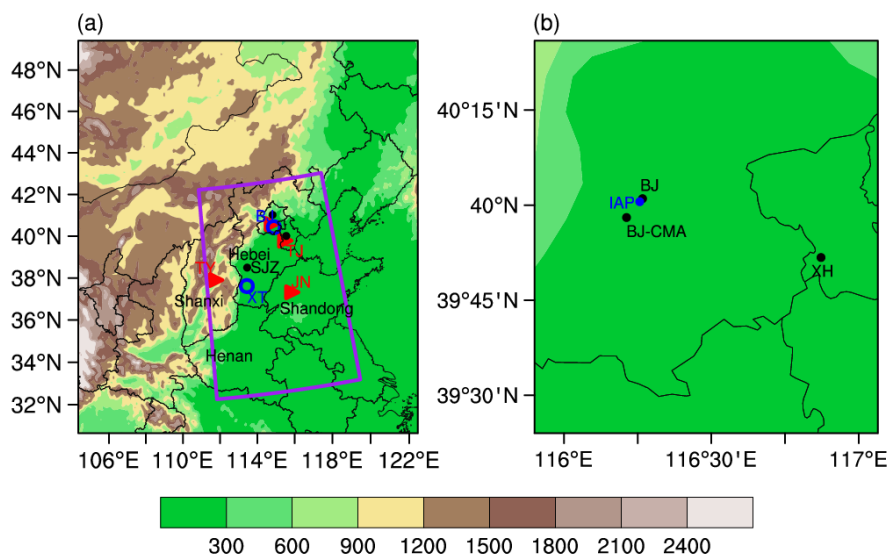
762



763 Table 2. Mean bias of downward SW radiation at surface ( $\text{W m}^{-2}$ ) and Net radiation  
764 at surface ( $\text{W m}^{-2}$ ) from NoAero and Aero relative to observation during daytime  
765 (averaged 0800 to 1800 LT) and nighttime (averaged 1900 to 0700 LT), averaged  
766 from 6<sup>th</sup> to 11<sup>th</sup> Dec. 2015 at Beijing, Tianjin, Taiyuan and Jinan respectively.

767

Station	SW radiation		Net radiation			
	Daytime		Daytime		Nighttime	
	NoAero	Aero	NoAero	Aero	NoAero	Aero
Beijing	149.4	38.0	102.2	15.0	-33.6	-33.2
Tianjin	115.5	70.9	72.2	36.4	-27.1	-26.4
Taiyuan	155.0	118.3	66.9	43.2	-33.6	-33.3
Jinan	149.1	97.7	81.2	45.3	-30.3	-29.3



768

769 Figure 1. (a) The model domain and the terrain height (shadings, m). Purple box

770 denotes the NCP, triangles are the observational sites of radiation (BJ: Beijing, TJ:

771 Tianjin, TY: Taiyuan and JN: Jinan), circles are sites of sounding observation (BJ:

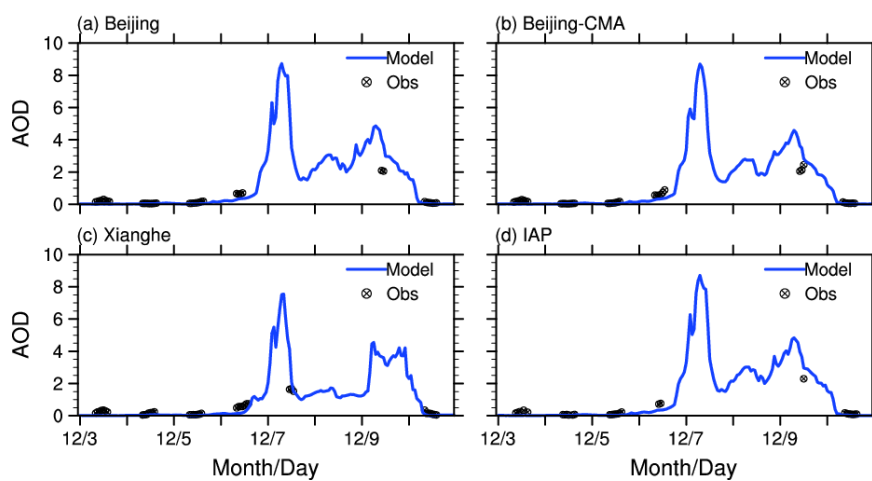
772 Beijing and XT: Xingtai), dots denote the major cities for validation of PM<sub>2.5</sub> (BJ:

773 Beijing, SJZ: Shijiazhuang and TJ: Tianjin). Names of provinces are also added

774 (Hebei, Shanxi, Shandong and Henan). (b) The observational sites of AOD,

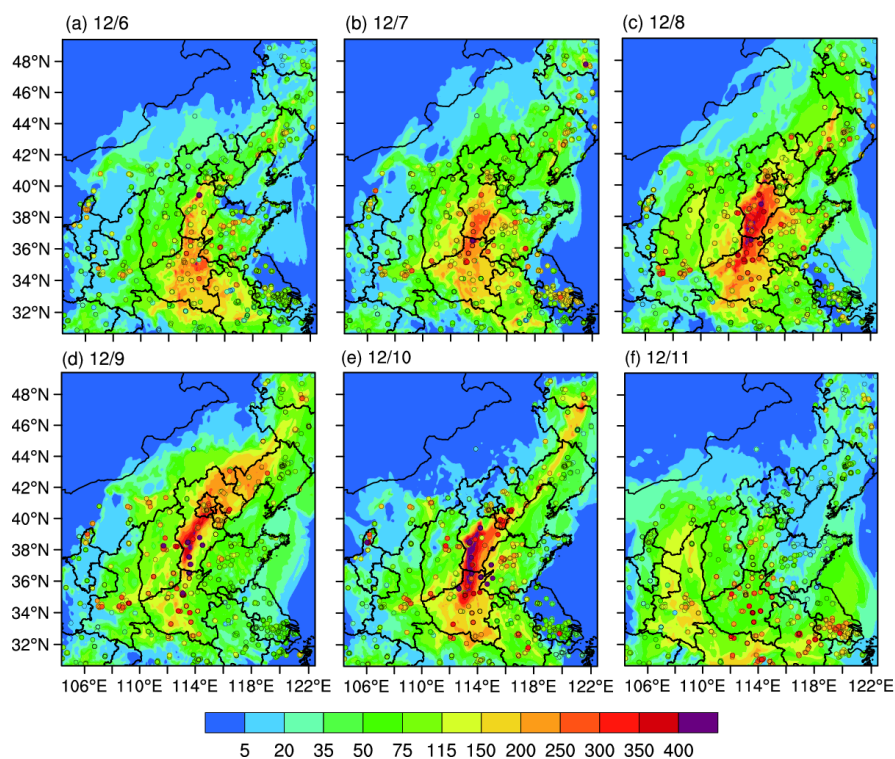
775 including AERONET sites (black dots, BJ: Beijing, BJ-CMA: Beijing-CMA and XH:

776 Xianghe) and IAP in-situ (blue dot) site.



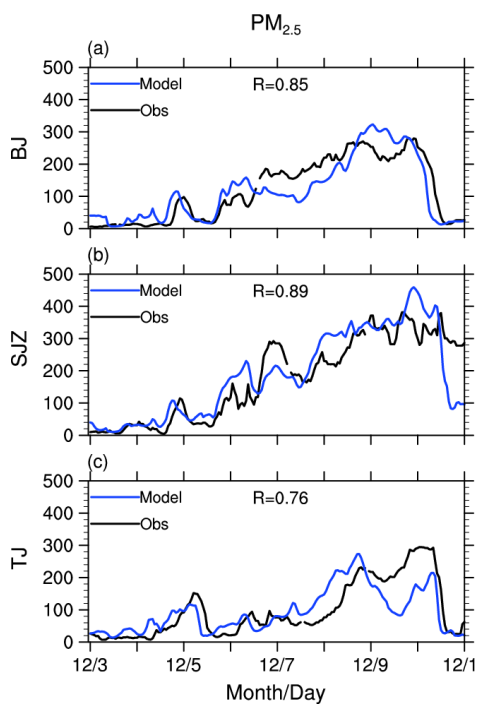
777

778 Figure 2. Temporal variation of observed (black dots) and simulated (blue) AOD at  
779 550nm during 3<sup>rd</sup>-10<sup>th</sup> Dec. (LT) at (a) Beijing, (b) Beijing-CMA, (c) Xianghe and (d)  
780 IAP, AOD observations are from (a-c) AERONET and (d) IAP in-situ site.



781

782 Figure 3. Observed (colored dots) and WRF-Chem simulated (shadings) spatial  
783 distribution of PM<sub>2.5</sub> concentrations ( $\mu\text{g m}^{-3}$ ) on 0800LT of (a) 6<sup>th</sup>, (b) 7<sup>th</sup>, (c) 8<sup>th</sup>, (d)  
784 9<sup>th</sup>, (e) 10<sup>th</sup> and (f) 11<sup>th</sup> Dec. respectively.



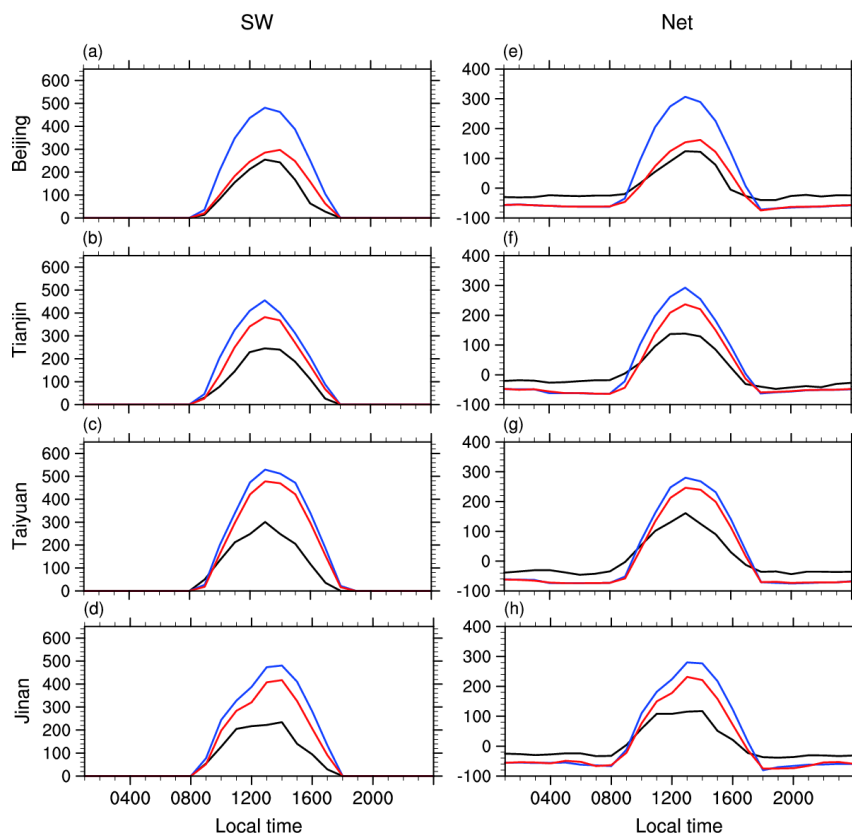
785

786 Figure 4. Observed (black) and WRF-Chem simulated (blue) temporal variation of

787  $PM_{2.5}$  ( $\mu\text{g m}^{-3}$ ) at three major cities: (a) Beijing (BJ), (b) Shijiazhuang (SJZ) and (c)

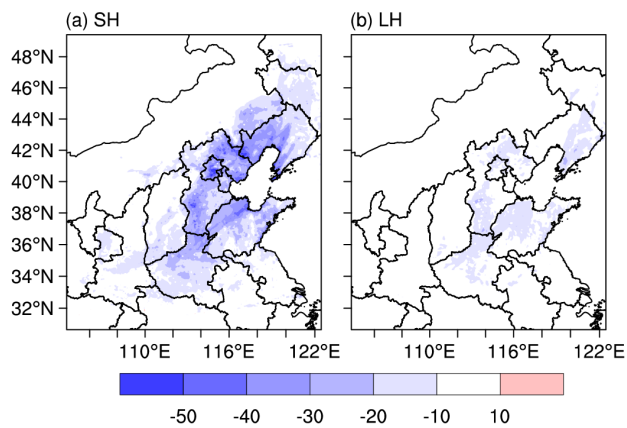
788 Tianjin (TJ).





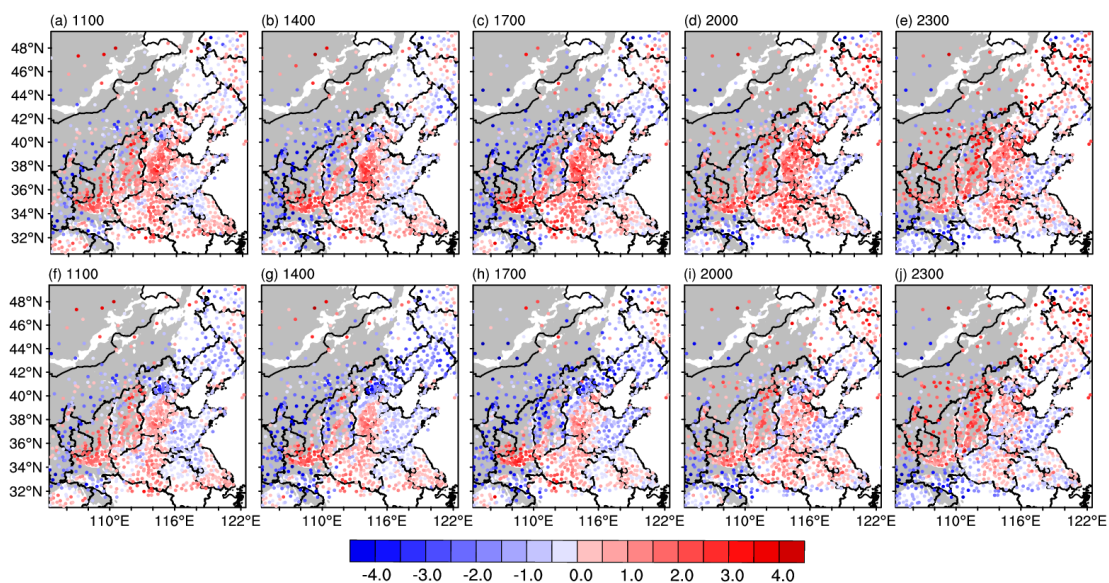
795

796 Figure 6. (a–d) observed (black) and simulated (NoAero: blue, Aero: red) diurnal  
797 cycles of downward shortwave radiation at surface ( $\text{W m}^{-2}$ ) averaged from 6<sup>th</sup> to 10<sup>th</sup>  
798 Dec. 2015 at (a) Beijing, (b) Tianjin, (c) Taiyuan and (d) Jinan, respectively. (e–h)  
799 are same with (a–d), but for net radiation at surface ( $\text{W m}^{-2}$ ).



800

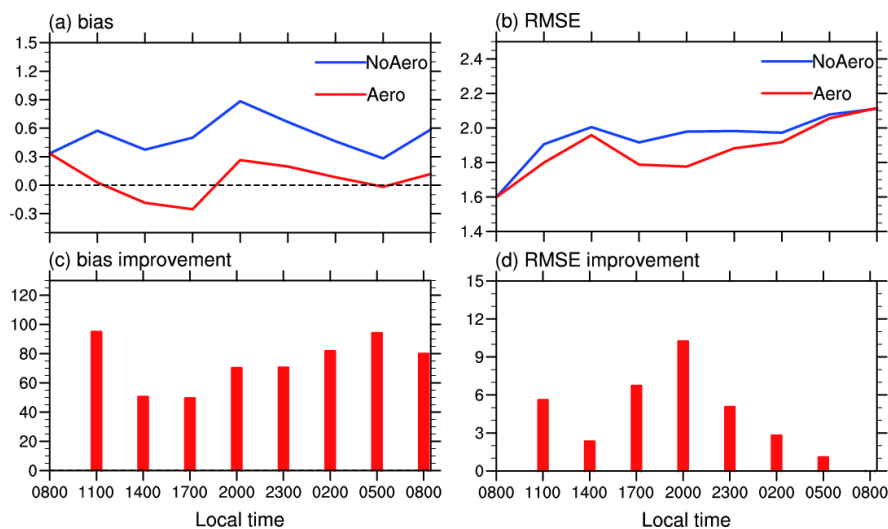
801 Figure 7. The differences (Aero minus NoAero) of (a) surface sensible heat flux and  
802 (b) surface latent heat flux ( $\text{W m}^{-2}$ , upward is positive) at 1300LT averaged from  
803 6th to 10th Dec. 2015.



804

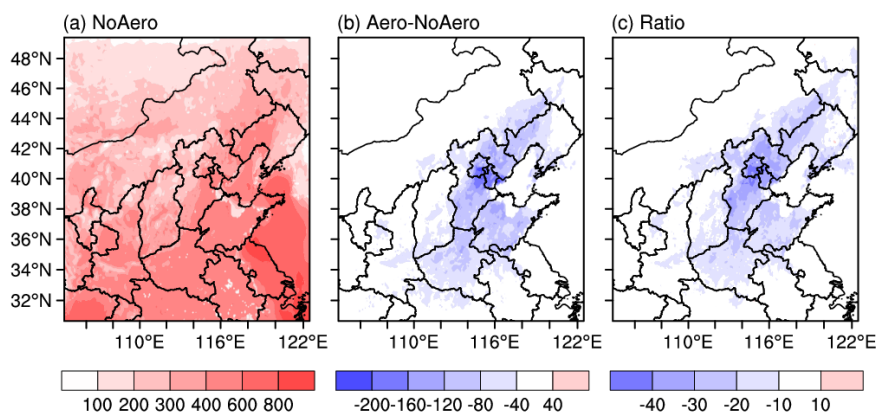
805 Figure 8. The bias of 2-m temperature ( $^{\circ}\text{C}$ ) at (a) 1100, (b) 1400, (c) 1700, (d) 2000 and (e) 2300 LT in NoAero averaged from 6th to 10th Dec

806 2015, (f–j) are same with (a–e), but for Aero. The grey areas denote the areas of terrain height above 1000m.



807

808 Figure 9. Area-averaged (a) bias and (b) RMSE of simulated 2-m temperature ( $^{\circ}\text{C}$ )  
809 in NoAero (blue) and Aero (red) over NCP area (defined in Fig. 1a), averaged from  
810 6<sup>th</sup> to 10<sup>th</sup> Dec. 2015, and the mean improvement (%) of (c) absolute value of bias  
811 and (d) RMSE in Aero relative to NoAero.

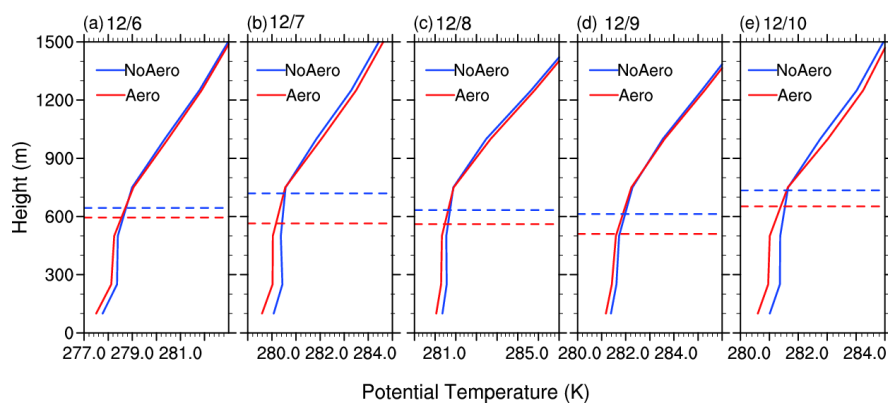


812

813 Figure 10. Daytime mean PBLH (m) in NoAero, (b) the difference between Aero

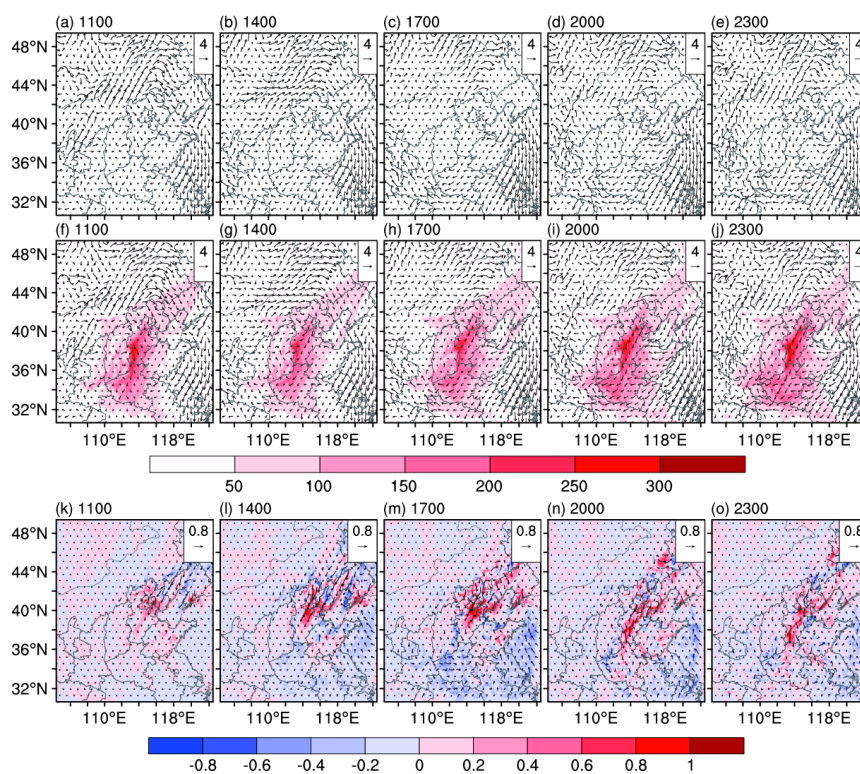
814 and NoAero (Aero minus NoAero) and (c) the ratio of changes (%) averaged during

815 6<sup>th</sup> to 10<sup>th</sup> Dec. 2015.



816

817 Figure 11. NCP (defined in Fig. 1a) area-averaged vertical profiles of potential  
818 temperature (K, solid) and planetary boundary-layer height (m, dash) in NoAero  
819 (blue) and Aero (red) at 1400 LT of (a) 6<sup>th</sup>, (b) 7<sup>th</sup>, (c) 8<sup>th</sup>, (d) 9<sup>th</sup> and (e) 10<sup>th</sup> Dec.  
820 2015.



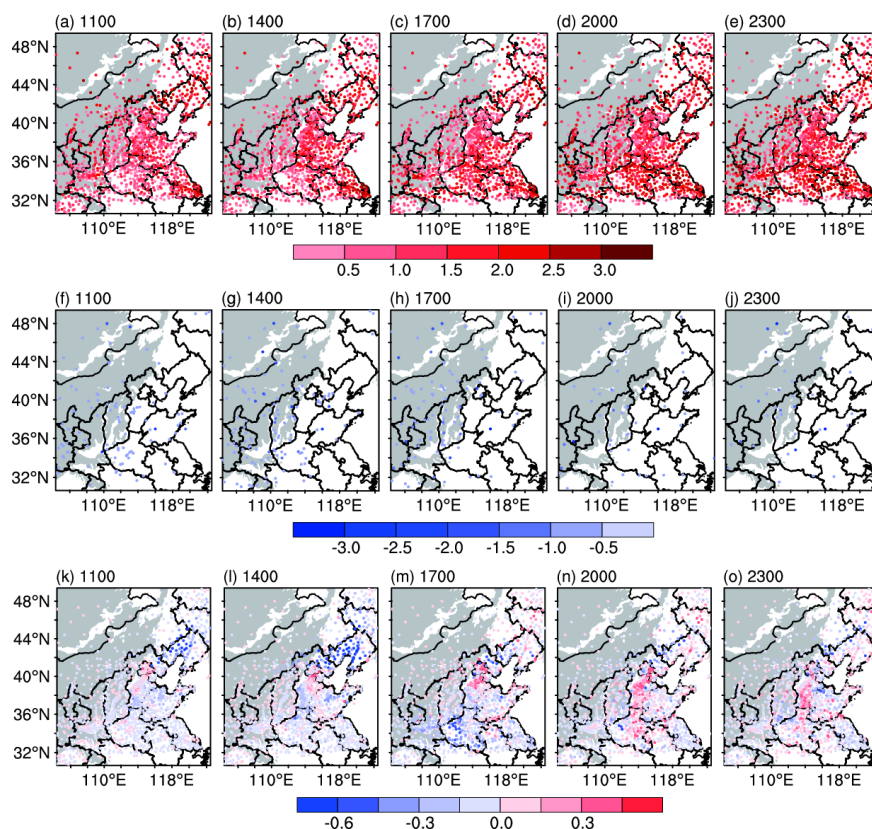
821

822 Figure 12. The 10m wind (vector) at 1100, 1400, 1700, 2000 and 2300 LT in (a–e)

823 NoAero and (f–j) Aero averaged during 6<sup>th</sup> to 10<sup>th</sup> Dec. 2015, shadings in (f–j) are

824 simulated PM<sub>2.5</sub> concentrations ( $\mu\text{g m}^{-3}$ ). (k–o) the difference of 10m wind (vector)

825 and wind speed (shadings) between Aero and NoAero (Aero minus NoAero).



826

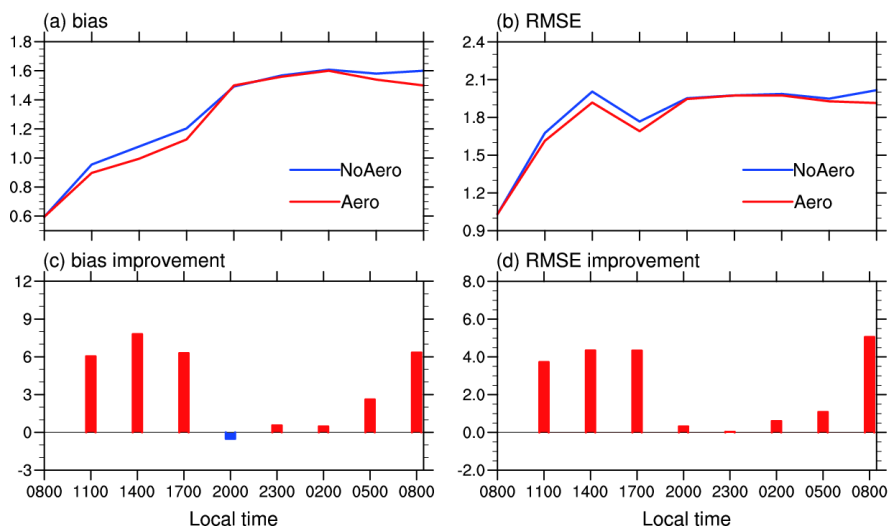
827 Figure 13. The bias of 10m wind speed ( $\text{m s}^{-1}$ ) at 1100, 1400, 1700, 2000 and 2300

828 LT for (a–e) overestimated sites and (f–j) underestimated sites in NoAero averaged

829 during 6<sup>th</sup> to 10<sup>th</sup> Dec. 2015. (k–o) the difference of absolute value of bias ( $\text{m s}^{-1}$ )

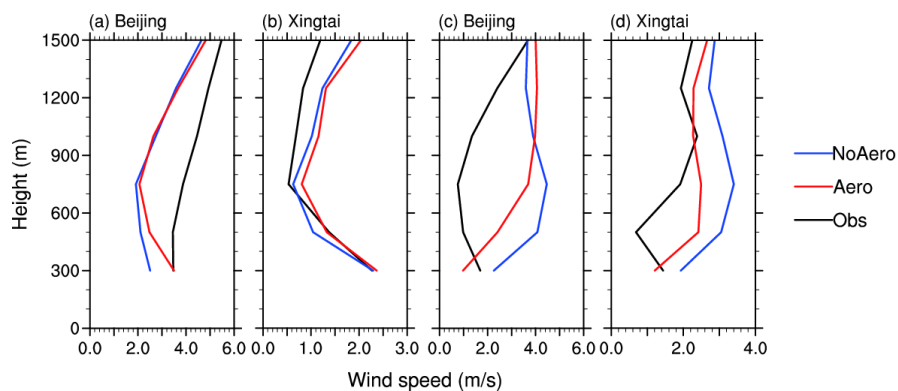
830 between Aero and NoAero (Aero minus NoAero). The grey areas denote the areas of

831 terrain height above 1000m.



832

833 Figure 14. Same with Fig.9, but for wind speed at 10m ( $\text{m s}^{-1}$ ).

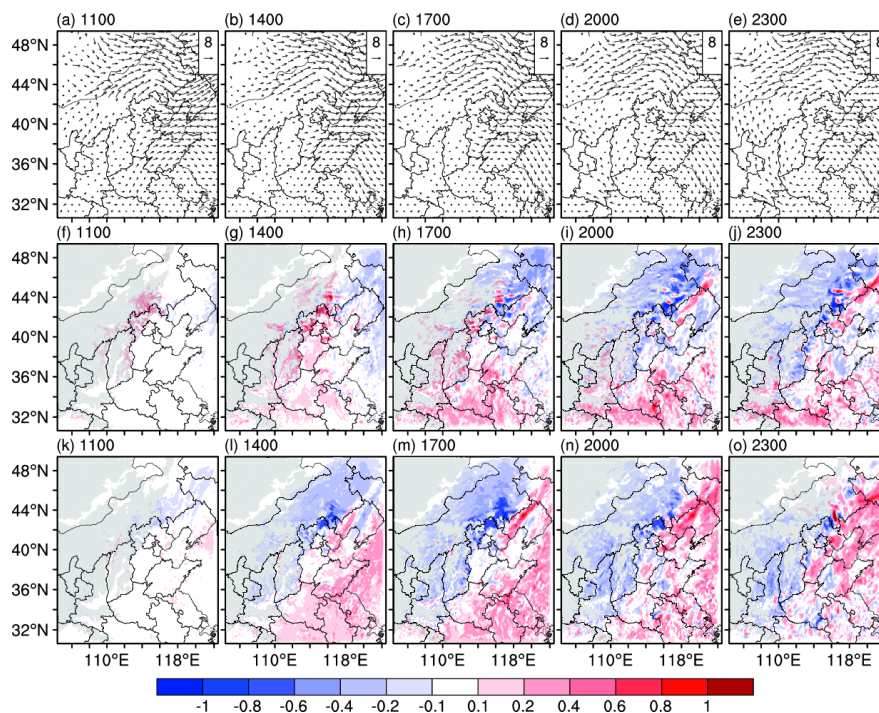


834

835 Figure 15. (a–b) Observed (black) and simulated (NoAero: blue, Aero: red) vertical

836 profiles of atmospheric wind speed ( $\text{m s}^{-1}$ ) at (a) Beijing and (b) Xingtai at 0800LT

837 averaged from 6<sup>th</sup> to 10<sup>th</sup> Dec., (c–d) are same with (a–b), but at 2000LT.



838

839 Figure 16. The wind at 850hPa (vector) at 1100, 1400, 1700, 2000 and 2300 LT in  
840 NoAero averaged during 6<sup>th</sup> to 10<sup>th</sup> Dec. 2015. The difference of (f–j) U and (k–o) V  
841 wind speed between Aero and NoAero (Aero minus NoAero). The grey areas denote  
842 the areas of terrain height above 1000m.